photonics

MDPI

Article

Visible Light-Range Quasi-Bound States in the Continuum in Symmetric Gold Nanohole Arrays for High-FOM Refractive-Index Sensing

Peiyi Lu [1,2], Weiwei Liu [3,*] and Silin Yang [2,4]

[1] School of Physics, South China Normal University, Guangzhou 510631, China
[2] PhotonSense Technology (Shenzhen) Co., Ltd., Shenzhen 518055, China
[3] Peng Cheng Laboratory (PCL), Shenzhen 518000, China
[4] College of Physics and Optoelectronic Engineering, Shenzhen University, Shenzhen 518060, China
* Correspondence: liuww@pcl.ac.cn

Abstract

Realizing high-quality-factor (high-Q) plasmonic resonances in the visible regime is critical for enhancing light-matter interactions and advancing biochemical sensing. However, traditional localized surface plasmon resonances (LSPRs) typically suffer from broad spectral linewidths due to severe radiative damping. In this work, we propose a simple two-dimensional symmetric gold nanohole-array metasurface that supports a symmetry-protected bound state in the continuum (SP-BIC) at normal incidence. By introducing extrinsic symmetry breaking via oblique incidence, this non-radiative dark state is successfully transformed into an observable high-Q quasi-BIC Fano resonance. Cartesian multipole decomposition reveals that this sharp mode ($\lambda \approx 688$ nm) is predominantly driven by a tightly confined Magnetic Dipole (MD) excitation, which drastically suppresses radiative leakage compared to the highly damped Electric Dipole (ED)-dominated LSPR. Consequently, the quasi-BIC mode exhibits an ultra-narrow spectral linewidth (FWHM $\approx$ 17.4 nm). While its bulk sensitivity (236.9 nm/RIU) is slightly lower than that of the LSPR mode, the exceptionally sharp resonance yields a remarkably low Limit of Detection (LOD) of 7.35×10^{-3} RIU, achieving a nearly five-fold improvement over the traditional LSPR. Furthermore, the quasi-BIC mode maintains an outstanding Figure of Merit (FOM up to $\sim$19.7 RIU^{-1}) across the entire sensing range. By eliminating the need for complex asymmetric nanofabrication, this robust angle-tuned design strategy provides a highly promising platform for the development of high-resolution, low-cost optical biosensors.

Keywords: bound states in the continuum; plasmonic metasurfaces; refractive-index sensing; magnetic dipole

Check for updates

Received: 12 February 2026
Revised: 3 April 2026
Accepted: 13 April 2026
Published: 21 April 2026

Copyright: © 2026 by the authors. Licensee MDPI, Basel, Switzerland. This article is an open access article distributed under the terms and conditions of the Creative Commons Attribution (CC BY) license.

1. Introduction

Biosensors capable of rapid response, high precision, and real-time on-site detection are increasingly demanded in biochemical analysis and related monitoring scenarios [1,2]. Optical sensing platforms are particularly attractive because subtle environmental perturbations can be directly transduced into measurable spectral signatures, enabling compact and label-free detection. However, practical plasmonic sensors often face a fundamental tension between strong near-field enhancement for boosted light–matter interaction and sufficiently

narrow linewidths for high-resolution readout, motivating resonant micro-/nano-photonic designs that can simultaneously enhance confinement and spectral sharpness.

Metasurfaces—two-dimensional planar materials composed of subwavelength artificial atoms—have emerged as a frontier in modern photonics due to their exceptional capability to manipulate the amplitude, phase, and polarization of electromagnetic waves at the nanoscale [3–5]. These engineered structures have demonstrated profound versatility across a wide spectrum of electromagnetic applications. For instance, metasurfaces have been extensively developed for broadband perfect absorption and efficient solar energy harvesting using refractory metals and cavity-based architectures [6,7]. Furthermore, by integrating active media such as vanadium dioxide (VO_2) or graphene, dynamically reconfigurable metasurfaces have been successfully realized for tunable thermal emission and dual-band camouflage [8,9]. While these energy-harvesting and active-modulation applications typically exploit strong, broadband optical absorption, practical optical biochemical sensing operates on a fundamentally different requirement: it strictly demands extremely narrow spectral linewidths (i.e., high Quality factors) to achieve high-resolution readout of subtle environmental perturbations.

Among various material systems, plasmonic metasurfaces have attracted significant attention because they can excite Surface Plasmon Polaritons (SPPs) and Localized Surface Plasmon Resonances (LSPRs), enabling sub-diffraction light localization and strong near-field enhancement [10,11]. These advantages underpin applications such as Surface-Enhanced Raman Scattering (SERS) [12], biochemical sensing [13], and nonlinear optics [14]. Nevertheless, metallic resonators in the visible band suffer from severe intrinsic losses, including non-radiative ohmic dissipation and radiative scattering into free space, which typically lead to low Q-factors and broadened resonance linewidths [15]. This loss-induced spectral broadening limits further improvement of plasmonic devices that require high precision.

To suppress radiative leakage and obtain sharper resonances, bound states in the continuum (BICs) have recently garnered widespread interest [16]. First proposed by von Neumann and Wigner [17], BICs are non-radiating eigenstates embedded in the radiation continuum. In optical metasurfaces, symmetry-protected or momentum-matched BIC modes can be realized through appropriate unit-cell parameter tuning, theoretically yielding vanishing radiative loss and infinite Q-factors [18]. In practical devices, perturbations (e.g., symmetry breaking) convert ideal BICs into quasi-BIC resonances with finite but ultrahigh Q, often manifested as sharp Fano lineshapes [19,20].

Current high-Q BIC studies are dominated by all-dielectric metasurfaces (e.g., silicon, silicon nitride) because dielectric materials exhibit negligible absorption in the visible and near-infrared regimes [21–23]. Koshelev et al. established an inverse-square dependence of Q on the asymmetry parameter in asymmetric dielectric metasurfaces, providing important guidance for high-Q device design [24]. In contrast, BIC research in metallic systems remains relatively limited and is largely concentrated in the microwave or terahertz regimes [25,26]. Although ohmic losses in metals impose an upper bound on Q, plasmonic BIC architectures can offer a distinct advantage by tightly confining fields at metal surfaces or within nanogaps, yielding exceptionally high local enhancement factors [27,28] that are valuable for strong light–matter interactions.

Realizing metallic BICs in the visible range is challenging due to strong interband-transition absorption and ohmic losses in noble metals (e.g., Au, Ag) [29]. Existing attempts typically employ hybrid plasmonic–photonic schemes assisted by high-index dielectric layers [30] or metallic grating platforms; for instance, visible-range BICs and their strong coupling with lattice modes have been reported in 1D MIM gratings using even-parity modes [31]. Moreover, quasi-BIC excitation in plasmonic metasurfaces most commonly relies on intrinsic symmetry breaking by designing geometrically asymmetric unit cells

(e.g., asymmetric split rings, deformed dimers) [32,33]. By comparison, extrinsic symmetry breaking (e.g., oblique incidence) in simple, in-plane symmetric two-dimensional (2D) metallic nanohole arrays has been less explored despite their mechanical robustness and richer lattice-resonance modal landscape.

Fundamentally, the formation of the symmetry-protected BIC (SP-BIC) in such symmetric structures can be understood through the lens of multipolar resonances. At strictly normal incidence, the incident electromagnetic field excites anti-parallel displacement currents within the metallic unit cell. Due to the rigorous in-plane structural symmetry, these currents induce strongly confined multipolar modes—predominantly an out-of-plane Magnetic Dipole (MD)—whose far-field radiation perfectly cancels out due to exact destructive interference. This renders the mode completely uncoupled from the free-space radiation continuum, forming a non-radiative "dark" SP-BIC state. However, by introducing extrinsic symmetry breaking via oblique incidence, a spatial retardation phase is established across the unit cell. This phase gradient disrupts the perfect balance of the multipolar radiation, opening a controlled radiative leakage channel. Consequently, the non-radiative SP-BIC is transformed into an observable, high-Q quasi-BIC Fano resonance that is fundamentally driven by the highly localized MD excitation.

Guided by this underlying multipolar mechanism, in this work, we propose and numerically investigate a periodic gold nanohole-array metasurface on a silica substrate. Unlike intrinsic symmetry-breaking designs, our structure preserves in-plane symmetry and exploits angular modulation, along with environmental refractive-index tuning, to study the coexistence and spectral evolution of broadband LSPR and narrowband quasi-BIC resonances in the visible regime. The results show that the symmetric nanohole array simultaneously supports both resonances with clearly differentiated refractive index responses: the LSPR mode exhibits pronounced spectral shifts, whereas the quasi-BIC mode maintains a high Q-factor with characteristic linewidth evolution. This dual-mode behavior—combining strong LSPR field intensity and quasi-BIC spectral sharpness within a unified architecture—clarifies the interplay between distinct plasmonic mechanisms in metallic nanohole arrays and suggests a promising route toward high-performance refractive-index sensing.

2. Materials and Methods

2.1. Unit Cell Design

As shown in Figure 1, the metasurface designed in this work consists of a periodic array of gold (Au) nanoholes deposited on a silica (SiO_2) substrate. The unit cells are arranged periodically with C_4 rotational symmetry. The structural parameters are defined as follows: The period $P = 450$ nm, the gold film thickness $H = 100$ nm, and the circular nanohole diameter $D = 260$ nm. The silica substrate is treated as a lossless medium in the visible range with a refractive index of $n_{SiO_2} = 1.45$. The dielectric permittivity of gold is taken from the experimental data of Johnson and Christy, which accurately accounts for the real part dispersion and imaginary part absorption losses in the visible band. The structure is covered with a liquid analyte, with an initial environmental refractive index set to $n = 1.33$ (simulating a water environment).

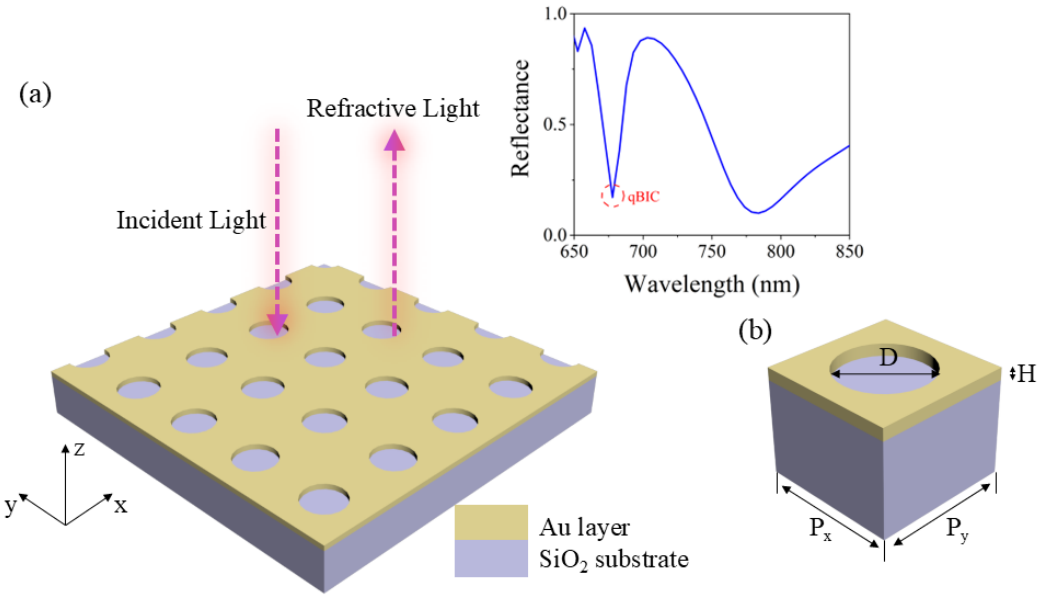


Figure 1. Schematic illustration of the proposed symmetric gold nanohole array metasurface. (**a**) 3D perspective view of the unit cell under plane wave illumination. The structure consists of a gold film with circular nanoholes on a silica substrate. (**b**) Top view and cross-sectional view of the unit cell. The geometric parameters are as follows: period $P = 450$ nm; hole diameter $D = 260$ nm; and gold thickness $H = 100$ nm. The refractive index of the silica substrate is $n_{SiO_2} = 1.45$.

2.2. Simulation Settings

Numerical simulations were performed using the Finite-Difference Time-Domain (FDTD) method (Lumerical FDTD Solutions). Periodic boundary conditions were applied in the x and y directions to simulate an infinite 2D array, while Perfectly Matched Layers (PMLs) were used in the z direction to fully absorb outgoing waves and eliminate boundary reflections. A broadband plane wave source was incident from above the structure. To investigate the angular dependence of the BIC, the incident angle θ was scanned from -15° to 15° in the $x-z$ plane. Reflectance spectra and electromagnetic field distributions were recorded using frequency-domain field monitors located above the structure. In our simulations, the reflectance (R) spectra were calculated by placing power monitors at the boundaries above the metasurface, respectively. All collected spectral powers were rigorously normalized to the incident light source. Throughout this manuscript, the optical responses are consistently evaluated and plotted based on the reflectance spectra.

3. Results and Discussion

3.1. Angle-Resolved Spectra and Verification of BIC Mechanism

To reveal the existence and physical origin of the BIC mode in this symmetric structure, we first investigated the optical properties of the gold nanohole array in momentum space. The angle-resolved reflectance spectra calculated by FDTD are presented in Figure 2c,d. The incident angle θ is related to the in-plane wave vector $k_{||}$ via the relation:

$$k_{||} = \frac{2\pi}{\lambda} \sin\theta, \tag{1}$$

where λ is the wavelength, and θ is the incident angle.

From Figure 2c, it can be clearly observed that for $n = 1.33$, a flat resonance band exists around the wavelength of 688 nm. Notably, at the Γ point (i.e., $\theta = 0^\circ$, marked by the white dashed line), this mode disappears completely from the spectrum. This implies that the mode cannot be excited by a normally incident plane wave, indicating that it is perfectly

decoupled from the far-field radiation continuum, corresponding to a typical symmetry-protected BIC (SP-BIC) state. Similarly, in Figure 2d, when $n = 1.40$, the resonance peak appears at 705 nm due to the red-shift induced by the increased environmental refractive index, while the ideal BIC state persists at the Γ point.

To quantitatively validate this characteristic BIC behavior, we extracted the evolution of the quality factor (Q-factor) as the system transitions from the ideal SP-BIC to the quasi-BIC state with increasing incidence angle θ, as shown in Figure 2a,b. At strictly normal incidence ($\theta = 0°$), the Q-factor theoretically diverges to infinity, representing a bound state with zero radiation leakage. By introducing extrinsic symmetry breaking via oblique incidence ($\theta > 0°$), a radiative channel is opened, transforming the dark state into an observable high-Q quasi-BIC Fano resonance. Crucially, the extracted Q-factor decays rapidly as the incidence angle increases, perfectly following the inverse quadratic relationship ($Q \propto sin^{-2}\theta$) that represents a universal theoretical hallmark of symmetry-protected BICs. This angle-dependent evolution unambiguously confirms the physical origin of the resonance and provides a robust mechanism to achieve highly tunable, high-Q resonances in the visible regime by simply manipulating the incident angle.

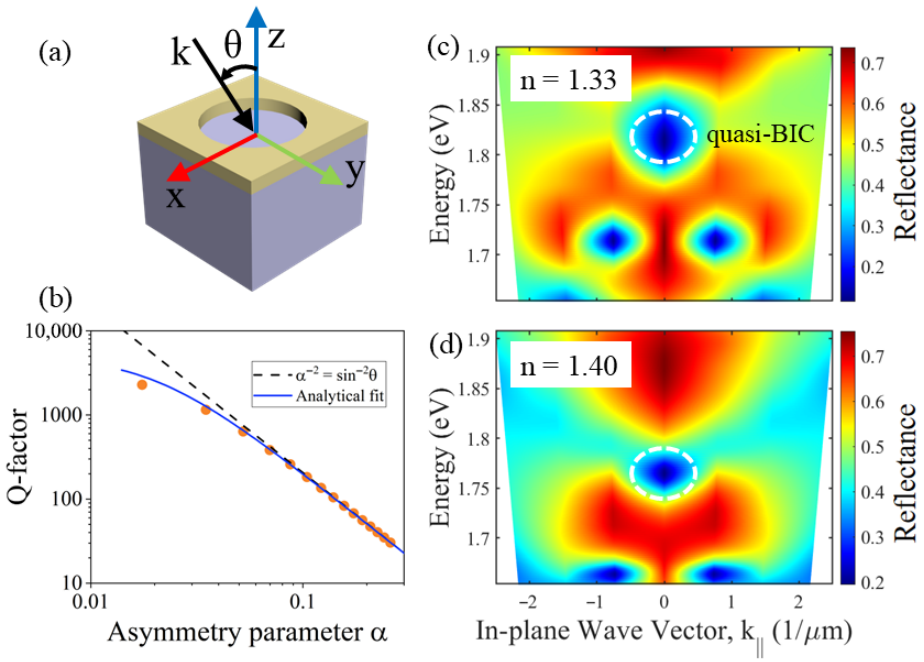


Figure 2. Excitation and characteristic evolution of the quasi-BIC mode via extrinsic symmetry breaking. (**a**) Schematic illustration of the oblique incidence configuration, where θ represents the incident angle. (**b**) Extracted Q-factor as a function of the asymmetry parameter α (related to $\sin\theta$). The dashed black line indicates the ideal inverse-square dependence characteristic of BIC behavior, and the solid blue line represents the analytical fit. (**c**,**d**) Angle-resolved reflectance dispersion maps for environmental refractive indices of (**c**) $n = 1.33$ and (**d**) $n = 1.40$. The white dashed circles explicitly mark the locations of the quasi-BIC modes, respectively.

As the incident angle gradually increases from 0°, the symmetry of the excitation source is broken, and the original dark mode transforms into a bright mode with a finite line width. As shown in the dispersion diagram, the quasi-BIC mode exhibits a distinct evolution: The resonance dip becomes sharper and shallower as $|k_{||}|$ decreases. The decreasing line width and deep modulation depth at the Γ-point confirm that the mode completely decouples from the free-space radiation, a signature of ideal BIC. This phenomenon is caused by the gradual closing of the radiation channel as symmetry is restored. It should be pointed out that due to the unavoidable intrinsic ohmic losses of metals in the visible range, even in the

ideal BIC state where radiative loss is fully suppressed, the absorption loss of the system remains. Therefore, the observed resonance manifests as a plasmonic quasi-BIC mode with a remarkably high Q-factor under normal incidence. This configuration is particularly advantageous for practical applications, as it significantly simplifies optical alignment and the experimental setup compared to oblique-incidence schemes.

3.2. Multipole Decomposition and Physical Mechanism

To gain deeper insight into the microscopic physical origins and the underlying light-matter interaction mechanisms of the quasi-BIC mode, we performed a Cartesian multipole decomposition based on the induced current density distribution $\mathbf{J}(\mathbf{r})$ within the unit cell. Figure 3a illustrates the scattered power contributions from the dominant fundamental multipole moments—namely, the electric dipole (ED) and magnetic dipole (MD)—as a function of wavelength. Note that the contributions from higher-order multipoles (such as quadrupoles) are intrinsically negligible in this subwavelength regime and are therefore excluded for clarity.

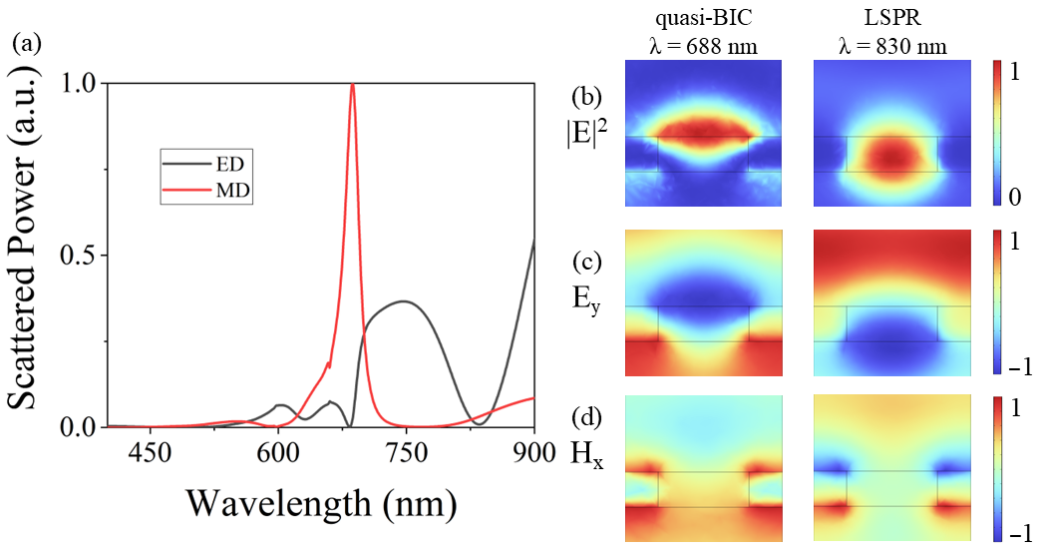


Figure 3. Multipole decomposition and normalized near-field distributions calculated at an oblique incidence angle of $\theta = 5°$. (**a**) Cartesian multipole decomposition of the scattered power spectra, demonstrating the dominance of the tightly confined Magnetic Dipole (MD, red curve) at the quasi-BIC resonance ($\lambda \approx 688$ nm) and the highly radiative Electric Dipole (ED, black curve) at the LSPR mode ($\lambda \approx 830$ nm). Higher-order multipoles are omitted due to their negligible scattered power contributions in this subwavelength regime. (**b**–**d**) Cross-sectional profiles in the $x-z$ planefor (**b**) the normalized electric field intensity ($|E|^2/|E_{max}|^2$), (**c**) the x-component of the electric field ($E_y/|E_{y,max}|$), and (**d**) the y-component of the magnetic field ($H_x/|H_{x,max}|$) for the quasi-BIC (**top** panels) and LSPR (**bottom** panels) modes. To ensure a rigorous physical comparison, all color maps for both modes are strictly normalized to the maximum absolute values of the quasi-BIC state (i.e., unified to $[0,1]$ for $|E|^2$ and $[-1,1]$ for E_y and H_x).

At the extremely sharp quasi-BIC resonance ($\lambda \approx 688$ nm), the scattering spectrum is unambiguously dominated by the Magnetic Dipole (MD, red curve) excitation. The MD scattered power exhibits a prominent peak that significantly surpasses the broad background radiation of the Electric Dipole (ED, black curve). Physically, this originates from the formation of strong anti-parallel circulating displacement currents driven by the extrinsic symmetry breaking, which induces a robust magnetic moment perpendicular to the structural plane. This strong magnetic light-matter confinement directly contributes to the ultra-high Q-factor and drastically suppresses radiative leakage.

In contrast, around the LSPR wavelength ($\lambda \approx 830$ nm), the multipole scattering spectrum exhibits no sharp enhancement. Instead, the optical response merges into a broad, heavily damped background predominantly sustained by the ED component. Without the strong local confinement provided by the MD excitation, the energy of the LSPR mode is severely depleted by intrinsic radiative scattering and non-radiative ohmic dissipation. This lack of strong resonant scattering enhancement perfectly explains its highly diffuse near-field distribution, extremely low Q-factor, and excessively broad spectral linewidth.

To visualize the local field enhancement capability, which is vital for high-resolution sensing, we extracted the cross-sectional near-field distributions for both the quasi-BIC and LSPR modes, as shown in Figure 3b–d. For a rigorous and direct comparison, the electromagnetic fields of both modes are strictly normalized to the absolute maximum value of the quasi-BIC state. As clearly depicted in the normalized electric field intensity profiles ($|E|^2/|E_{max}|^2$) [Figure 3b], the quasi-BIC mode achieves the maximum normalized intensity of 1, tightly confined within and near the edges of the gold nanohole. Under the exact same color scale, the maximum intensity of the LSPR mode is remarkably lower. Furthermore, the instantaneous field components E_y and H_x [Figure 3c,d], normalized to $[-1, 1]$, demonstrate that the quasi-BIC mode supports a highly localized and symmetric field profile bound to the metallic surface, effectively avoiding radiation into free space. Conversely, the LSPR fields are highly diffuse, further corroborating their heavily damped radiative nature and inherently lower sensing Figure of Merit.

3.3. Refractive Comparison of Index Sensing Performance

Based on the robust local field enhancement of the quasi-BIC mode, we comprehensively investigated its performance as a refractive-index sensor and benchmarked it against the traditional LSPR mode. Figure 4a illustrates the simulated reflectance spectra under a specific oblique incidence angle of $\theta = 5°$ as the environmental refractive index (n) increases from 1.33 to 1.40. A pronounced and highly regular red-shift of the extremely sharp resonance dip is observed, shifting smoothly from 688 nm to 705 nm. This excellent linearity is crucial for reliable biosensor calibration.

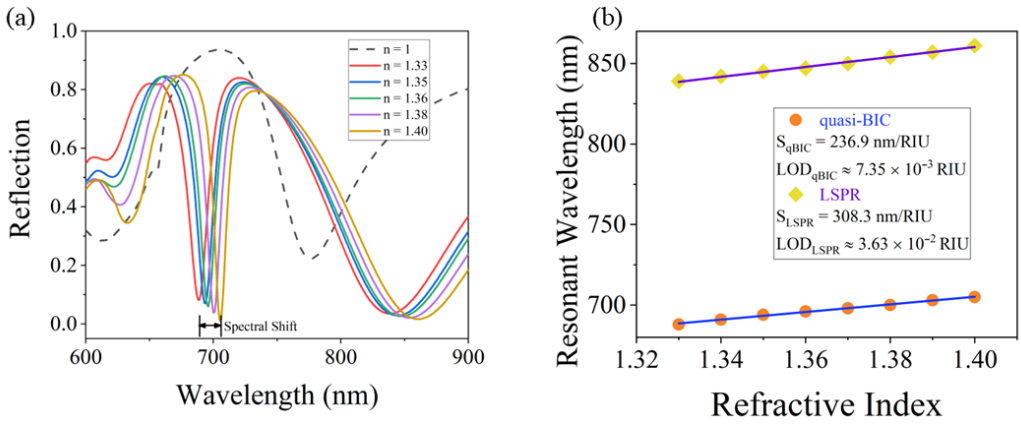


Figure 4. Refractive index sensing performance and Limit of Detection (LOD) analysis under an oblique incidence of $\theta = 5°$. (**a**) Reflectance spectra of the quasi-BIC mode as the environmental refractive index (n) increases from 1.33 to 1.40, showing a regular and sharp red-shift. (**b**) Linear fitting of the resonance wavelength versus the refractive index for the quasi-BIC (orange circles) and LSPR (yellow squares) modes. Despite a slightly lower bulk sensitivity ($S = 236.9$ nm/RIU), the quasi-BIC mode achieves an LOD of 7.35×10^{-3} RIU, which is nearly 5 times superior to that of the LSPR mode (3.63×10^{-2} RIU) owing to its ultra-narrow FWHM.

To quantitatively evaluate the sensing capabilities, we extracted the resonance wavelengths and performed linear fitting to determine the bulk sensitivity ($S = \Delta\lambda/\Delta n$), as shown in Figure 4b. The LSPR mode exhibits a bulk sensitivity of 308.3 nm/RIU (where RIU stands for Refractive Index Unit), which is slightly higher than that of the quasi-BIC mode (236.9 nm/RIU). Nevertheless, as Altug et al. have comprehensively emphasized [34], relying exclusively on bulk sensitivity to evaluate advanced optical biosensors provides an incomplete picture. The true performance and practical resolution of a sensor are determined by the Limit of Detection (LOD), which inherently depends on the interplay between the sensitivity and the resonance linewidth (FWHM). For a theoretical analysis without specific experimental system noise, the LOD is a theoretical estimate based on an assumed spectral resolution, which is generally approximated as LOD $\approx$ FWHM/$(10 \times S)$.

Thanks to its ultra-narrow linewidth (FWHM $\approx$ 17.4 nm), the quasi-BIC mode achieves a remarkably low LOD of 7.35×10^{-3} RIU. In stark contrast, despite its higher sensitivity, the LSPR mode suffers from severe radiative damping, resulting in an excessively broad linewidth (FWHM $\approx$ 112.0 nm) and a significantly poorer LOD of 3.63×10^{-2} RIU. This nearly five-fold improvement in the LOD rigorously demonstrates that the sharp quasi-BIC resonance provides an overwhelming advantage in detecting minute refractive index variations, easily compensating for its slightly lower bulk sensitivity.

3.4. Analysis of Quality Factor and Figure of Merit

To further establish the superiority of the quasi-BIC mode across the entire sensing range, we calculated the Quality factor (Q-factor) and the Figure of Merit (FOM $= S/\text{FWHM}$), as summarized in Figure 5.

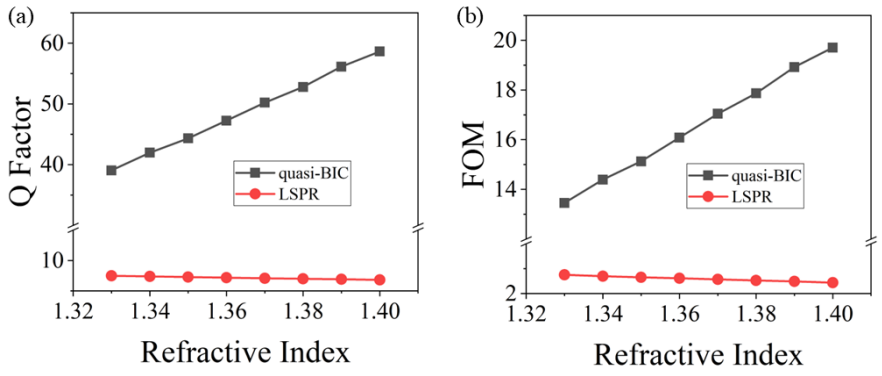


Figure 5. Comparison of the Figure of Merit (FOM) and Quality factor (Q-factor) between the quasi-BIC and LSPR modes. (**a**) The FOM (FOM $= S/\text{FWHM}$) as a function of the refractive index. The quasi-BIC mode (red line) consistently maintains a high FOM between 13.5 and 19.7 RIU^{-1}, whereas the LSPR mode (blue line) remains poor at $\sim$2.5 RIU^{-1}. (**b**) The Q-factor evolution. The quasi-BIC mode exhibits a high Q-factor that increases with the refractive index, while the LSPR mode is heavily damped with a constant low Q-factor of $\sim$7.

As depicted in Figure 5b, the quasi-BIC mode exhibits significantly higher Q-factors (ranging from $\sim$39 to $\sim$59) that remarkably increase with the environmental refractive index. This trend reflects the robust light-matter confinement of the magnetic dipole-dominated mode. Conversely, the Q-factor of the LSPR mode remains clamped at a very low value ($\sim$7) across the entire index range due to its intrinsic radiative losses. Consequently, as shown in Figure 5a, the FOM of the quasi-BIC mode spans from 13.5 to 19.7 RIU^{-1}, massively outperforming the LSPR mode (FOM $\approx$ 2.5 RIU^{-1}). These decisive metrics confirm that the proposed quasi-BIC metasurface offers dramatically enhanced spectral resolution and sensing fidelity, proving its immense potential for high-performance, label-free biochemical sensing.

4. Conclusions

In summary, we have numerically demonstrated a highly sensitive metasurface refractive-index sensor based on a simple, symmetric gold nanohole array operating in the visible regime. Our angle-resolved spectral analysis strictly confirms that the structure supports a symmetry-protected BIC (SP-BIC) at normal incidence. By simply introducing an oblique incidence angle to induce extrinsic symmetry breaking, this non-radiative dark state is successfully transformed into a high-Q quasi-BIC Fano resonance. Cartesian multipole decomposition reveals that this sharp resonance is fundamentally driven by a tightly confined Magnetic Dipole (MD) excitation, which drastically suppresses radiative leakage compared to the highly damped Electric Dipole (ED)-dominated LSPR mode.

Consequently, the quasi-BIC mode exhibits an ultra-narrow spectral linewidth (FWHM $\approx$ 17.4 nm) and an exceptionally strong normalized local field enhancement. Sensing performance evaluations demonstrate that while the quasi-BIC mode possesses a slightly lower bulk sensitivity ($S = 236.9$ nm/RIU) than the LSPR mode, its exceptionally narrow linewidth yields a remarkable Limit of Detection (LOD) of 7.35×10^{-3} RIU—an improvement of nearly a factor of five over the traditional LSPR mode. Furthermore, the quasi-BIC mode maintains a high Q-factor (up to $\sim$59) and an outstanding Figure of Merit (FOM up to $\sim$19.7 RIU^{-1}) across the entire testing range, massively outperforming the heavily degraded LSPR. Crucially, this design completely eliminates the necessity for complex nanofabrication of asymmetric unit cells. By achieving high-resolution reliable sensing solely through the tuning of the incident angle, this simple yet robust strategy offers a highly promising platform for the development of next-generation, low-cost optical biosensors and active plasmonic devices.

Author Contributions: Conceptualization, W.L.; Methodology, P.L. and W.L.; Software, W.L. and S.Y.; Validation, P.L., W.L. and S.Y.; Formal analysis, P.L. and W.L.; Investigation, W.L.; Resources, W.L.; Data curation, P.L. and S.Y.; Writing—original draft, P.L. and W.L.; Writing—review & editing, P.L., W.L. and S.Y.; Supervision, W.L.; Project administration, W.L.; Funding acquisition, W.L. All authors have read and agreed to the published version of the manuscript.

Funding: This research was funded by National Natural Science Foundation of China grant number 62005181.

Data Availability Statement: The data presented in this study are available on request from the corresponding author.

Conflicts of Interest: Authors Peiyi Lu and Silin Yang were employed by the company PhotonSense Technology (Shenzhen) Co., Ltd. The remaining authors declare that the research was conducted in the absence of any commercial or financial relationships that could be construed as a potential conflict of interest.

References

1. Zhao, X.; Guo, Z.; Zhou, Y.; Guo, J.; Liu, Z.; Luo, M.; Li, Y.; Wang, Q.; Zhang, M.; Yang, X.; et al. Highly sensitive, modification-free, and dynamic real-time stereo-optical immuno-sensor. *Biosens. Bioelectron.* **2023**, *237*, 115477. [CrossRef] [PubMed]
2. Guo, Z.; Qin, Y.; Chen, P.; Hu, J.; Zhou, Y.; Zhao, X.; Liu, Z.; Fei, Y.; Jiang, X.; Wu, X. Hyperboloid-Drum Microdisk Laser Biosensors for Ultrasensitive Detection of Human IgG. *Small* **2020**, *16*, 2000239. [CrossRef] [PubMed]
3. Yu, N.; Capasso, F. Flat optics with designer metasurfaces. *Nat. Mater.* **2014**, *13*, 139–150. [CrossRef] [PubMed]
4. Kildishev, A.V.; Boltasseva, A.; Shalaev, V.M. Planar photonics with metasurfaces. *Science* **2013**, *339*, 1232009. [CrossRef]
5. Genevet, P.; Capasso, F.; Aieta, F.; Khorasaninejad, M.; Devlin, R. Recent advances in planar optics: From plasmonic to dielectric metasurfaces. *Optica* **2017**, *4*, 139–152. [CrossRef]
6. Ai, Z.; Yi, Y.; Yang, H.; Liu, M.; Yi, Y.; Tang, C.; Gao, F. TiN-Ti ultra-broadband solar absorber: Efficient heat absorption and high thermal stability. *Phys. Lett. A* **2025**, *556*, 130827. [CrossRef]
7. Liu, H.; Li, J.; Yang, H.; Wang, J.; Li, B.; Zhang, H.; Yi, Y. TiN-Only Metasurface Absorber for Solar Energy Harvesting. *Photonics* **2025**, *12*, 443. [CrossRef]

8. Ai, Z.; Yang, H.; Liu, M.; Cheng, S.; Wang, J.; Tang, C.; Gao, F.; Li, B. Phase-Transition-Enabled Dual-Band Camouflage in VO2/Ag Multilayered Nanostructures. *Phys. E Low-Dimens. Syst. Nanostruct.* **2025**, *173*, 116327. [CrossRef]
9. Chen, Z.; Liu, M.; Cheng, S.; Wang, J.; Yi, Y.; Li, B.; Tang, C.; Gao, F. Bilayer Graphene Metasurface with Dynamically Reconfigurable Terahertz Perfect Absorption. *Curr. Appl. Phys.* **2025**, *80*, 282–290. [CrossRef]
10. Meinzer, N.; Barnes, W.L.; Hooper, I.R. Plasmonic meta-atoms and metasurfaces. *Nat. Photonics* **2014**, *8*, 889–898. [CrossRef]
11. Barnes, W.L.; Dereux, A.; Ebbesen, T.W. Surface plasmon subwavelength optics. *Nature* **2003**, *424*, 824–830. [CrossRef]
12. Langer, J.; de Aberasturi, D.J.; Aizpurua, J.; Alvarez-Puebla, R.A.; Auguié, B.; Baumberg, J.J.; Bazan, G.C.; Bell, S.E.; Boisen, A.; Brolo, A.G.; et al. Present and future of surface-enhanced Raman scattering. *ACS Nano* **2019**, *14*, 28–117. [CrossRef] [PubMed]
13. Brolo, A.G. Plasmonics for future biosensors. *Nat. Photonics* **2012**, *6*, 709–713. [CrossRef]
14. Kauranen, M.; Zayats, A.V. Nonlinear plasmonics. *Nat. Photonics* **2012**, *6*, 737–748. [CrossRef]
15. Khurgin, J.B. How to deal with the loss in plasmonics and metamaterials. *Nat. Nanotechnol.* **2015**, *10*, 2–6. [CrossRef]
16. Hsu, C.W.; Zhen, B.; Stone, A.D.; Joannopoulos, J.D.; Soljačić, M. Bound states in the continuum. *Nat. Rev. Mater.* **2016**, *1*, 16048. [CrossRef]
17. von Neumann, J.; Wigner, E. Über merkwürdige diskrete Eigenwerte. *Phys. Z.* **1929**, *30*, 465–467.
18. Marinica, D.; Borisov, A.; Shabanov, S. Bound states in the continuum in photonics. *Phys. Rev. Lett.* **2008**, *100*, 183902. [CrossRef]
19. Rybin, M.V.; Koshelev, K.L.; Sadrieva, Z.F.; Samusev, K.B.; Bogdanov, A.A.; Limonov, M.F.; Kivshar, Y.S. High-Q supercavity modes in subwavelength dielectric resonators. *Phys. Rev. Lett.* **2017**, *119*, 243901. [CrossRef]
20. Limonov, M.F.; Rybin, M.V.; Poddubny, A.N.; Kivshar, Y.S. Fano resonances in photonics. *Nat. Photonics* **2017**, *11*, 543–554. [CrossRef]
21. Kuznetsov, A.I.; Miroshnichenko, A.E.; Brongersma, M.L.; Kivshar, Y.S.; Luk'yanchuk, B. Optically resonant dielectric nanostructures. *Science* **2016**, *354*, aag2472. [CrossRef]
22. Tittl, A.; Leitis, A.; Liu, M.; Yesilkoy, F.; Choi, D.Y.; Neshev, D.N.; Kivshar, Y.S.; Altug, H. Imaging-based molecular barcoding with pixelated dielectric metasurfaces. *Science* **2018**, *360*, 1105–1109. [CrossRef]
23. Han, K.; Liu, W.; Zhu, Z. High-sensitivity and Q-engineered all-dielectric metasurface sensor driven by bound states in the continuum. *J. Opt.* **2026**, *in press*. [CrossRef]
24. Koshelev, K.; Lepeshov, S.; Liu, M.; Bogdanov, A.; Kivshar, Y. Asymmetric metasurfaces with high-Q resonances governed by bound states in the continuum. *Phys. Rev. Lett.* **2018**, *121*, 193903. [CrossRef]
25. Singh, R.; Chowdhury, D.R.; Xiong, W.; Yang, H.; Azad, A.K.; Taylor, A.J.; O'Hara, J.F.; Chen, H.T. Ultrasensitive terahertz sensing with high-Q Fano resonances in metasurfaces. *Appl. Phys. Lett.* **2014**, *105*, 171101. [CrossRef]
26. Cong, L.; Singh, R. Symmetry-protected dual bound states in the continuum in metamaterials. *Adv. Opt. Mater.* **2019**, *7*, 1900383. [CrossRef]
27. Liang, Y.; Koshelev, K.; Zhang, F.; Lin, H.; Lin, S.; Kivshar, Y.; Jia, B. Bound states in the continuum in plasmonic metasurfaces. *Nanophotonics* **2020**, *9*, 2937–2950.
28. Azzam, S.; Shalaev, V.; Boltasseva, A.; Kildishev, A. Formation of bound states in the continuum in hybrid plasmonic-photonic systems. *Phys. Rev. Lett.* **2018**, *121*, 253901. [CrossRef] [PubMed]
29. Johnson, P.B.; Christy, R.W. Optical constants of the noble metals. *Phys. Rev. B* **1972**, *6*, 4370. [CrossRef]
30. Doeleman, W.M.; Monticone, F.; Hollander, W.; Alù, A.; Koenderink, A.F. Experimental observation of a polarization vortex at an optical bound state in the continuum. *Nat. Photonics* **2018**, *12*, 397–401. [CrossRef]
31. Yao, K.; Liu, Y. Plasmonic bound states in the continuum. *Nanoscale* **2018**, *10*, 8779–8786. [CrossRef] [PubMed]
32. Fedotov, V.; Rose, M.; Prosvirnin, S.; Papasimakis, N.; Zheludev, N. Sharp trapped-mode resonances in planar metamaterials with a broken structural symmetry. *Phys. Rev. Lett.* **2007**, *99*, 147401. [CrossRef] [PubMed]
33. Hao, F.; Sonnefraud, Y.; Van Dorpe, P.; Maier, S.A.; Halas, N.J.; Nordlander, P. Symmetry breaking in plasmonic nanocavities: Subradiant LSPR sensing and a tunable Fano resonance. *Nano Lett.* **2008**, *8*, 3983–3988. [CrossRef]
34. Tseng, M.L.; Jahani, Y.; Leitis, A.; Altug, H. Dielectric Metasurfaces Enabling Advanced Optical Biosensors. *ACS Photonics* **2021**, *8*, 47–60. [CrossRef]

Disclaimer/Publisher's Note: The statements, opinions and data contained in all publications are solely those of the individual author(s) and contributor(s) and not of MDPI and/or the editor(s). MDPI and/or the editor(s) disclaim responsibility for any injury to people or property resulting from any ideas, methods, instructions or products referred to in the content.